Focusing of Maneuvering High-Squint-Mode SAR Data Based on Equivalent Range Model and Wavenumber-Domain Imaging Algorithm

Zhenyu Li , Jianlai Chen , Wentao Du , Bing Gao, Deming Guo, Tao Jiang, Tao Wu, Huaigen Zhang, and Mengdao Xing , *Fellow, IEEE*

Abstract—Due to the complexity of high-squint synthetic aperture radar (SAR) mounted on maneuvering platforms, the traditional geometric model and imaging algorithms cannot be directly applied in the diving or climbing stage for the existence of vertical velocity. Aiming at this issue, an equivalent geometric model of maneuvering high-squint-mode SAR is constructed, and a modified wavenumber-domain imaging algorithm combined with the proposed equivalent range model is proposed in this article. First, the disadvantages of the conventional range model are analyzed in detail and an equivalent range model is proposed to describe the motion characteristic of squint SAR in maneuvering mode, which maintains the azimuth-shift invariance along the flight direction in the new slant range plane. Then, to achieve the requirement of maneuvering SAR real-time processing, a modified wavenumber-domain imaging algorithm with a high usage of the spectrum by axis rotation for high-squint SAR data is proposed. Further, since the equivalent model may introduce the severe distortion in the imaging plane, a novel geometric correction method based on inverse projection is performed to obtain the ground imagery with a little distortion. Finally, simulation and real-data processing results validate the superiority of the proposed algorithm.

Index Terms—Equivalent range model, geometric correction, high-squint mode, maneuvering synthetic aperture radar (SAR), wavenumber domain.

I. INTRODUCTION

SYNTHETIC aperture radar (SAR) [1], as an active microwave sensor, is widely mounted on maneuvering platforms (MPs), such as unmanned aerial vehicles [2], [3] and missiles [4], [5]. Compared with other motion platforms, the SAR sensors mounted on MPs have some special characteristics, such as flexible flight tracks, high-squint observation, and real-time

processing requirements [6]. Due to the flexible trajectories of these MPs, SAR usually works in a diving or climbing mode, i.e., maneuvering mode, and its flight height varies with the azimuth slow time, which makes the azimuth invariance questionable in the slant range plane [7]–[15]. In addition, a high-squint mode is often adopted to ensure advanced observation and repeated observations. Furthermore, since the resolution of full-aperture MPs SAR data far exceeds the anticipated requirements, sub-aperture data processing with a reasonable size has more advantages [11].

For the geometric model of maneuvers, a fast raw data simulation method for missile-borne SAR is proposed in the literature [16]. The impacts of acceleration in the 2-D frequency domain are analyzed, and the inverse process is used for imaging processing. However, this method uses many approximations and is only suitable for low squint angle and low resolution. Furthermore, works of literature [17]–[19] discuss the constant acceleration model for maneuvers on the basis of equivalence and divide the range model into two parts: one is the hyperbolic range model (HRM) without acceleration, the other is the term with acceleration. These equivalences simplify the subsequent imaging procedures and can be directly combined with the high-resolution imaging algorithms, such as Omega-K [20], [21]. Moreover, a fourth-order range model (FORM4 or DRM4 [22]), advanced hyperbolic range equation (AHRE) [23], [24], modified AHRE [25], improved range model [26], velocity equivalent model [27], and modified equivalent squint range model [28] are proposed for maneuvers with curved orbit. These models simplify the complex algebraic expression of the range model. However, it may sacrifice the accuracy of the range model since it only considers the equivalence of mathematical expression without analyzing real motion characteristics. For further applications, the imaging models and algorithms of high-resolution-high-squint SAR with a curved track will be the research emphasis and difficulty. In order to lay the groundwork, a squint maneuvering SAR range model and imaging algorithm without acceleration is studied, which brings great convenience for the following research on range model and algorithm in the case of a curved track.

For the imaging algorithms of high-squint SAR, chirp scaling (CS) [29], nonlinear chirp scaling (NLCS) [12], and their extensions are proposed [7]–[10], [17], [19], [30]–[32]. Based on the

four-order range model, these methods acquire the 2-D target spectrum by the method of series inversion first, and then construct the range and azimuth matching functions. However, they are only suitable for the small squint angle and low resolution. For high-resolution-high-squint mode, the wavenumber-domain algorithms adopt Stolt interpolation to correct the spatial-variant range cell migration (RCM), which can theoretically achieve accurate SAR imaging. Based on this advantage, Liang *et al.* [11] propose a modified Omega-K algorithm with a linear range walk correction (LRWC). However, LRWC will cause the azimuth dependence and all of the Doppler parameters vary with the azimuth position. Further, azimuth resampling, which is a good approach for correcting azimuth dependence without considering motion compensation (MoCo), is proposed to deal with the problem of azimuth dependence in [11]. The motion characteristics will be changed after resampling operation, it brings a great challenge for MoCo and affects the final focusing quality. For maneuvering SAR with a curved track, Li *et al.* [18] propose an extended Omega-K with the consideration of constant accelerations. This method acquires an approximation value of the real slant range history in order to establish a similar HRM for simplifying the subsequent imaging procedures. However, the proposed algorithm is not suitable for subaperture data processing and ignores the azimuth variance of targets as well as the range-variance of equivalent angles. In [33], a two-step frequency-domain imaging algorithm is proposed to adapt to subaperture data processing in diving mode. This method analyzes the vertical velocity on the range model and further increases the squint angle by squint minimization. On the contrary, the azimuth variance due to the correction of RCM via LRWC has a negative effect on the azimuth focus depth, so the algorithm is not suitable for high-resolution-high-squint mode. Besides, some other recent research works [34]–[41] on maneuvering high-squint-mode SAR discuss the impacts of the acceleration in detail, and LRWC is used to realize RCM correction with the effect of azimuth dependence. These publications are the modifications of CS and NLCS, which are all the frequency-domain imaging algorithms. Furthermore, the time-domain imaging algorithms, e.g., backprojection (BP) [42] and its modifications [43]–[47], can perfectly realize high-squint maneuvering SAR imaging without the consideration of computation and MoCo. Therefore, the time-domain imaging algorithms may not be suitable for maneuvering SAR in some scenarios.

In view of the aforementioned problems, the maneuvering SAR imaging not only needs to consider the real-time processing with subaperture data but also needs to combine an effective range model to simplify the whole imaging procedures. Considering the factors earlier, this article proposes a modified wavenumber-domain imaging algorithm combined with an equivalent range model. Compared with the referenced range model and imaging algorithms, the main advantages of the proposed algorithms are as follows. First, the proposed equivalent range model meets the azimuth-shift invariance on the new imaging plane. Second, the traditional MoCo methods [48]–[53] can be directly combined with the equivalent range model. Third, the equivalent range model paves the way for further research on
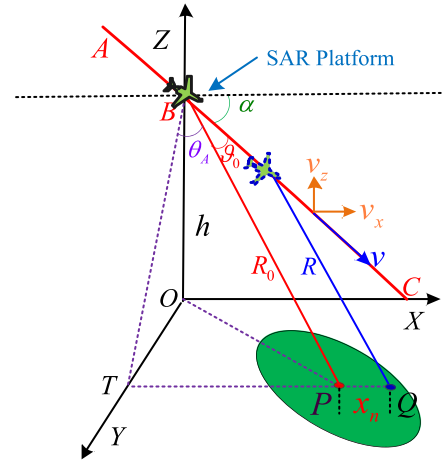

Fig. 1.   Geometric model of maneuvering high-squint-mode SAR.

the acceleration case. Fourth, the proposed algorithm is suitable for the high-resolution-high-squint mode.

The rest of the article is organized as follows. The disadvantages of the conventional range models are discussed and the new range model is established in Section II. In Section III, an imaging algorithm in the wavenumber domain is newly developed, under the circumstance of subaperture. In Section IV, the results of simulation and real data are presented to verify the proposed algorithm. Conclusions are drawn in Section V.

II. Geometric Model for Maneuvering High-Squint-Mode SAR

A geometric model of maneuvering high-squint-mode SAR is established, as shown in Fig. 1. The SAR platform flights along the straight line *ABC*. At the middle time during acquisition, *B* denotes the point of MP, *P* is the center point of antenna footprint, and *h* is the height of the platform at this moment. We suppose that there is an arbitrary point target denoted as *Q*, which shifts the azimuth position x_n in the same nearest range cell from center point *P*. R_0 is the slant range from radar to the center point *P*. The symbols α, θ_A, and ϑ_0 are the diving angle, squint angle, and forward angle, respectively. The instantaneous slant range of point *Q* can be expressed as

$$\boldsymbol{R}(t_m; R_0) = \sqrt{\begin{array}{c}(v_x t_m - R_0 \sin\theta_A - x_n)^2 + (h - v_z t_m)^2 \\ + (R_0^2 \cos^2\theta_A - h^2)\end{array}}$$

(1)

where t_m is the azimuth slow time, v_x is the velocity along *X*-axis, and v_z is the velocity along *Z*-axis. Note that the velocity along *Y*-axis is ignored since the velocities of east and north can be compounded into the 1-D velocity in the imaging model. In addition, the trajectory of the platform is assumed as a straight line without considering the accelerations.

A. Conventional Range Model and Its Disadvantages

According to the existing algorithms for squint SAR imaging [5]–[10], the instantaneous slant range is generally expanded

TABLE I
LIST OF SIMULATION PARAMETERS

System Parameters	Value	Motion Parameters	Value
Carrier frequency	17 GHz	Squint angle (θ)	70°
Pulse bandwidth	300 MHz	Altitude	6 km
Sampling frequency	360 MHz	Center slant range	40 km
Pulse duration	20 μs	Diving angle (α)	~26.6°
System PRF	2 KHz	Velocity of platform (v)	(0,200,-100) m/s

by Taylor series with respect to the azimuth slow-time t_m. Therefore, the expression of instantaneous slant range in (1) can be rewritten as

$$
\begin{aligned}
\boldsymbol{R}(t_m, R_0) = R_T &- \frac{hv_z + v_x x_n + R_0 v_x \sin\theta_A}{R_T} t_m \\
&+ \left(\frac{v_x^2 + v_z^2}{2R_T} - \frac{(hv_z + v_x x_n + R_0 v_x \sin\theta_A)^2}{2R_T^3} \right) t_m^2 \\
&+ \left(\begin{array}{c} \frac{(v_x^2 + v_z^2)(hv_z + v_x x_n + R_0 v_x \sin\theta_A)}{2R_T^3} \\ - \frac{(hv_z + v_x x_n + R_0 v_x \sin\theta_A)^3}{2R_T^5} \end{array} \right) t_m^3 + \cdots
\end{aligned}
\tag{2}
$$

where $R_T = \sqrt{R_0^2 + 2R_0 x_n \sin\theta_A + x_n^2}$. In (2), it is evident that the coefficients of the first-, second-, and third-order terms and the constant term R_T are all related to x_n. When $x_n = 0$, one can obtain $R_T = R_0$, which means that both the range curvature and azimuth matching factor vary with the azimuth position. In other words, all the coefficients in (2) are azimuth dependent and the assumption of azimuth-invariance is no longer valid. Specifically, the further the target's azimuth position from the center point, the greater dependence the range curvature mitigation and azimuth matching factors have. Besides, the imaging algorithms based on the conventional range model often adopt the reference range of center point to construct the range curvature mitigation correction and azimuth matching operation. This approximation may bring a large residual curvature and obvious azimuth defocusing for edge points. Thus, the imaging algorithms with the conventional range model may affect the azimuth focusing depth and lead to serious image defocusing.

In order to evaluate the residual azimuth-variance RCM and azimuth phase of the conventional range model, we rewrite the coefficients of $k_i(R_0)$ $i = 1, 2, 3$ in expression (2) as follows:

$$
\begin{cases}
k_1(R_0, x_n) = -\frac{hv_z + v_x x_n + R_0 v_x \sin\theta_A}{R_T} \\
k_2(R_0, x_n) = \frac{v_x^2 + v_z^2}{2R_T} - \frac{(hv_z + v_x x_n + R_0 v_x \sin\theta_A)^2}{2R_T^3} \\
k_3(R_0, x_n) = \frac{(v_x^2 + v_z^2)(hv_z + v_x x_n + R_0 v_x \sin\theta_A)}{2R_T^3} \\
\qquad - \frac{(hv_z + v_x x_n + R_0 v_x \sin\theta_A)^3}{2R_T^5}
\end{cases}
\tag{3}
$$

where $k_1(R_0)$, $k_2(R_0)$, and $k_3(R_0)$ denote the linear, quadratic, and cubic RCM terms, respectively. The residual RCM and

corresponding phase can be expressed as

$$
\begin{cases}
\Delta R_{\text{rcm}}(R_0, x_n) = \left(k_i(R_0, x_n) - k_i(R_0, x_n)|_{x_n=0} \right) \\
\left(\frac{T_a}{2} \right)^2, \qquad i = 1, 2, 3 \\
\Delta \varphi_{\text{rcm}}(R_0, x_n) = \frac{4\pi}{\lambda} \left(k_i(R_0, x_n) - k_i(R_0, x_n)|_{x_n=0} \right) \\
\left(\frac{T_a}{2} \right)^2, \qquad i = 1, 2, 3
\end{cases}
\tag{4}
$$

where T_a is the subaperture acquisition time and λ is the wavelength. For further analysis, the simulation parameters are listed in Table I. The radar works in Ku-band, the squint angle is 70°, and x_n is 1 km. Fig. 2(a)–(f) shows the envelope and phase errors of residual RCM terms caused by the conventional range model.

From Fig. 2, it is observed that the residual RCM and phase vary with the azimuth position heavily, and the variance increases with the distance from azimuth position to the center point. The variance of linear RCM between the edge point and the center point is almost 15 m, as shown in Fig. 2(a). According to the principle that the minimum envelope error can be neglected when its value is less than half of the resolution and the minimum phase error can be neglected when its value is less than $\pi/4$, the residual envelope and phase errors of the linear RCM term are obviously larger than the minimum value of the principle, as shown in Fig. 2(a) and (b). For the 0.5 m resolution requirement of the final focusing imagery, the residual envelope error of the quadratic RCM term is not satisfied but the residual envelope error of the cubic RCM term can be neglected, as shown in Fig. 2(c) and (e). However, the residual phase errors of quadratic RCM and cubic RCM are both larger than $\pi/4$, as indicated in Fig. 2(d) and (f).

In general, the imaging algorithms based on the conventional range model ignore the residual envelope and phase errors of high-order terms will cause defocusing in final imagery. The complex slant range model cannot be directly combined with some precise focusing algorithms, such as the wavenumber-domain imaging algorithm. A more accurate range model should be introduced for maneuvering high-squint-mode SAR.

B. Equivalent Range Model

Compared with the complex geometric model in Fig. 1, a simple model with the equivalence basic is proposed to ensure the accuracy and pave the way for the following precise algorithm. In this new model, the imaging plane consists of the velocity vector and slant range vector, as the dotted lines shown in Fig. 3. Let t_n be the center time when the beam center passes through the point target P, then the instantaneous range from P to radar
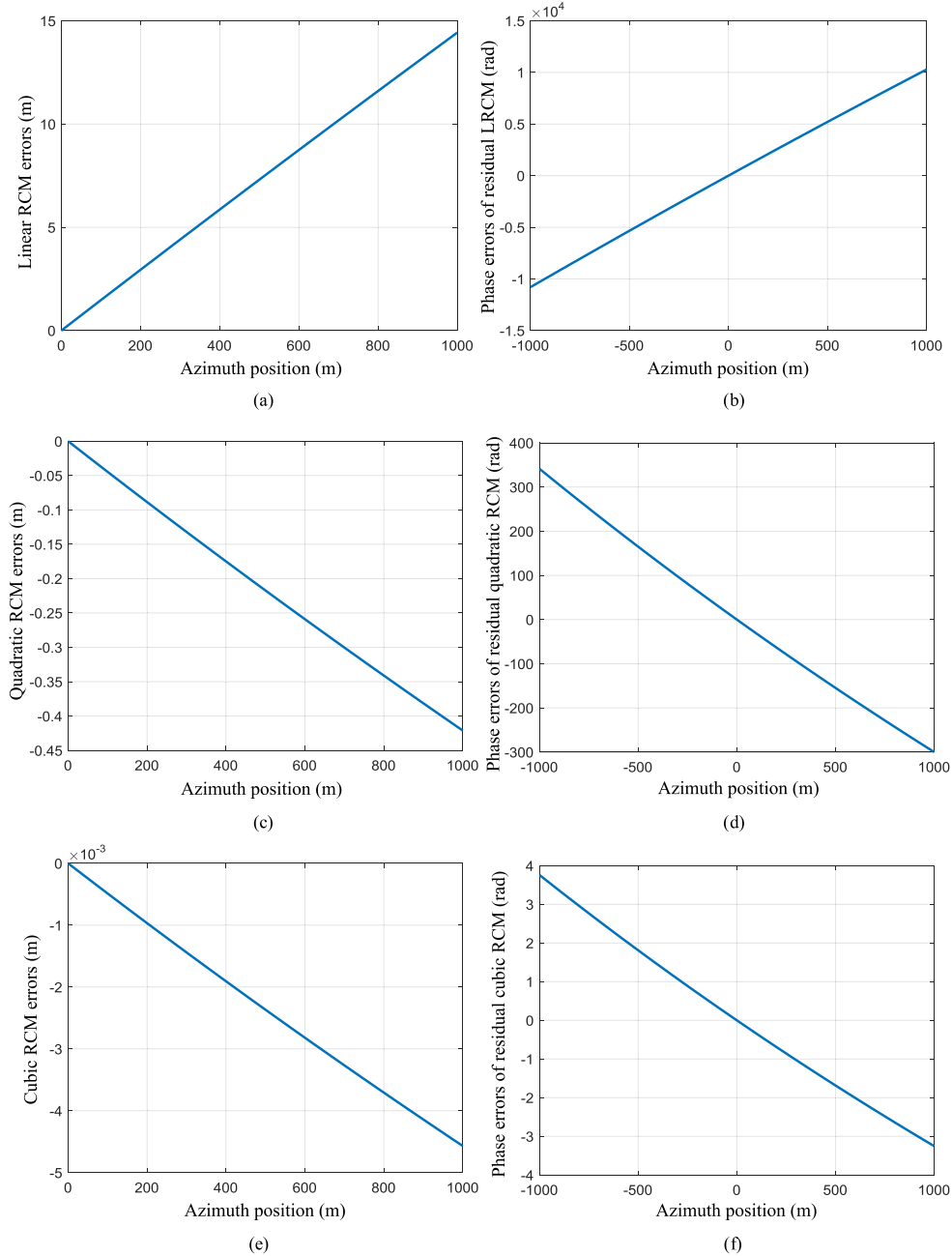
Fig. 2.   Envelope and phase errors of residual RCM terms. (a) and (b) Envelope and phase errors of residual linear RCM term. (c) and (d) Envelope and phase errors of residual quadratic RCM term. (e) and (f) Envelope and phase errors of residual cubic RCM term.

can be expressed as

$$R(t_m, R_0) = \sqrt{\begin{array}{l} R_0^2 + (v_x^2 + v_z^2)(t_m - t_n)^2 \\ -2R_0\left(v_x \sin\theta_A + \frac{h}{R_0}v_z\right)(t_m - t_n) \end{array}}. \quad (5)$$

Based on the geometric model in Fig. 3, $(v_x \sin\theta_A + hv_z/R_0)$ in (5) represents the projection of the velocity vector to the beam line of sight (LOS) and yields

$$v \sin\theta = v_x \sin\theta_A + \frac{h}{R_0}v_z \quad (6)$$

where $v = \sqrt{v_x^2 + v_z^2}$ is the resultant velocity, which is the velocity along the straight line ABC. θ represents the new squint angle in the equivalent range model, i.e., the angle $\angle DBP$ in Fig. 3. Therefore, (5) can be rewritten as

$$R(t_m, R_0) = \sqrt{R_0^2 + v^2(t_m - t_n)^2 - 2R_0 v \sin\theta\,(t_m - t_n)}. \quad (7)$$

For the conventional model in Fig. 1, the descending velocity existing on the plane BTP makes the property of the echo shift-variance in the X-direction. In comparison, the equivalent model established on the plane $BCPD$, an imaging plane that is spanned by the velocity vector and the beam sight vector, is
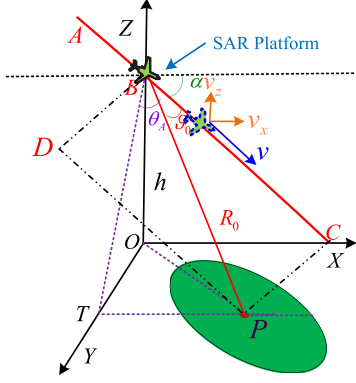
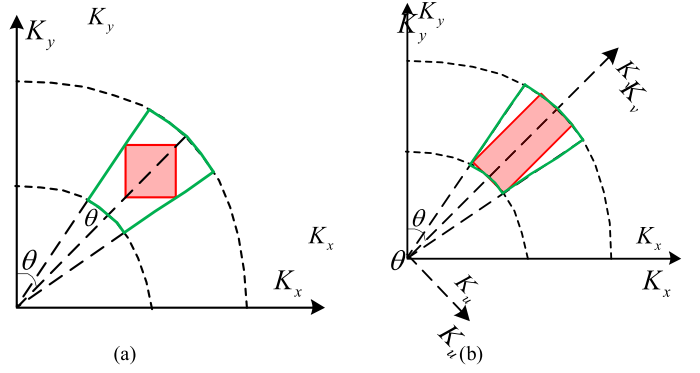Fig. 3. Equivalent range model for maneuvering high-squint-mode SAR.

Fig. 4. Selectable areas of spectrum support region before and after axis rotation. (a) Selectable area before axis rotation. (b) Selectable area after axis rotation.

azimuth shift-invariant in the direction of the velocity vector. Actually, the plane *BCPD* can be obtained via rotating the plane *BTP* along the *BP* axis. With this subtle equivalence, the imaging model of high-squint mode maneuvering SAR becomes azimuth-invariance on the new imaging plane *BCPD*, which facilitates the following precise imaging algorithm and MoCo [48]–[53]. Note that the corresponding imaging plane is rotated through the equivalent processing and this procedure will result in a large geometric distortion in the focused imagery. Therefore, the geometric correction is necessary during the imaging processing.

III. MODIFIED WAVENUMBER-DOMAIN IMAGING ALGORITHM

According to the aforementioned analysis, a modified wavenumber-domain imaging algorithm is proposed combined with the equivalent range model in this section. Suppose that the transmitted pulses are linelly frequency modulated. The received signal in the range wavenumber and azimuth time domain can be expressed as

$$Ss\left(K_r, t_m; R_0\right) = W_r\left(K_r\right) \cdot w_a\left(t_m\right)$$
$$\times \exp\left(-j\frac{(K_r - K_{rc})^2 c^2}{16\pi\gamma}\right) \exp\left(-jK_r \cdot \boldsymbol{R}\left(t_m; R_0\right)\right)$$
$$(8)$$

where γ is the range chirp rate of the transmitted signal and c is the light speed, f_c is the carrier frequency, K_r is the range wavenumber, $K_{rc} = 4\pi f_c/c$. $W_r(\cdot)$ and $w_a(\cdot)$ are the range windowing function in the wavenumber domain and the azimuth windowing function in the distance domain, respectively.

A. Range Preprocessing and Axis Rotation

In (8), the first exponential term corresponds to the range compression, and the second term is the azimuth modulation term. Therefore, the range compression factor is given by

$$H_{rc}\left(K_r\right) = \exp\left(j\frac{(K_r - K_{rc})^2 c^2}{16\pi\gamma}\right). \quad (9)$$

Afterward, we transform the range compressed signal into the 2-D wavenumber domain via the azimuth fast Fourier transform

(FFT) and yields

$$SS(K_r, K_x) = W_r\left(K_r\right) \cdot W_a\left(K_x\right)$$
$$\times \exp\left[\begin{array}{c} -jR_0\left(\sqrt{K_r^2 - K_x^2}\cos\theta + K_x\sin\theta\right) \\ -jK_x x_n \end{array}\right] \quad (10)$$

where K_x represents the azimuth wavenumber, $W_a(\cdot)$ is the azimuth windowing function in the wavenumber domain. In order to reduce the impacts of range curvature and azimuth frequency modulation, a bulk compensation factor at the reference range R_{ref} in the 2-D wavenumber domain is given by

$$H_{\text{rcm}}\left(K_r, K_x\right)$$
$$= \exp\left[j\left(\sqrt{K_r^2 - K_x^2}\cos\theta + K_x\sin\theta\right) \cdot R_{\text{ref}}\right]. \quad (11)$$

After the compensation, the signal is expressed as

$$SS\left(K_r, K_x; R_0\right) = W_r\left(K_r\right) \cdot W_a\left(K_x\right)$$
$$\times \exp\left[-j\sqrt{K_r^2 - K_x^2} \cdot y - jK_x \cdot x\right] \quad (12)$$

where $x = (R_0 - R_{\text{ref}})\sin\theta + x_n$ and $y = (R_0 - R_{\text{ref}})\cos\theta$. Observing (12), the expression of the 2-D spectrum is similar to the broadside SAR and the following core procedure is Stolt interpolation for solving range azimuth coupling in the wavenumber-domain imaging algorithms. In order to realize the interpolation, the selection of a rectangle region in the data support region is essential. However, a simple selection area is limited by a squint angle in the conventional algorithms, as shown in the relatively small shaded area in Fig. 4(a). Such strict limitation will evidently reduce the imaging quality, and make it difficult to meet the resolution requirement. For the imagery of squint SAR, the higher the squint angle, the smaller the support region. In order to enlarge the selected region of the spectrum and guarantee the resolution, Liang *et al.* [11] propose a modified Omega-K algorithm with the correction of RCM by squint minimization in the range frequency and azimuth time domain, but this method results in the variant range envelope and azimuth phase, and thus reduces the maximum depth of azimuth focusing. To avoid the issue of variance and realize the
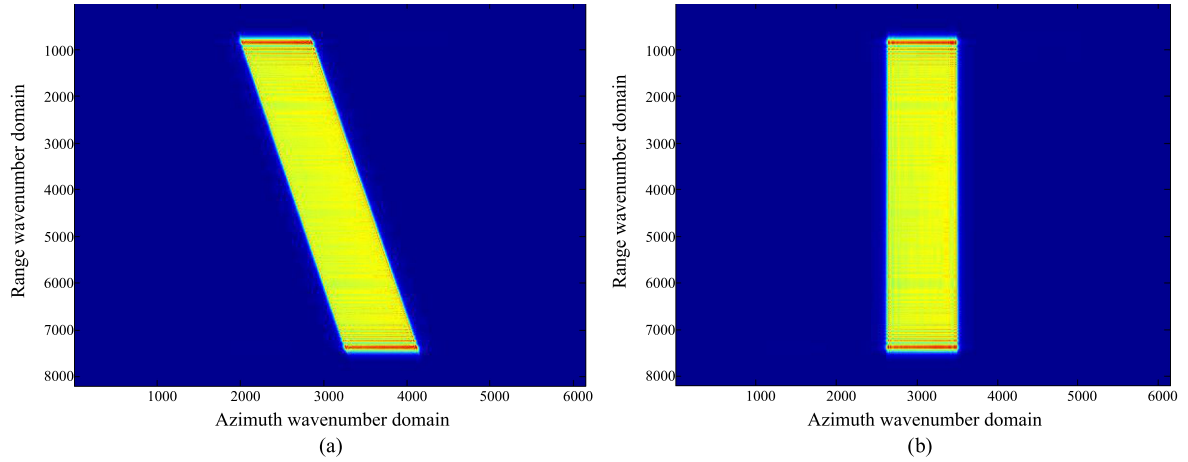
Fig. 5. Point target spectrum in squint mode before and after axis rotation. (a) Original spectrum before rotation. (b) Spectrum after rotation.

support region with maximum usage, an axis rotation operation is creatively performed for the squint SAR spectrum selection. The rotation angle is the squint angle. After being rotated, the spectrum is corrected into broadside mode along the LOS and cross LOS. Furthermore, the selectable area of the support region can be described as a rectangle region in the new coordinates, as shown in Fig. 4(b).

According to the above analysis, the rotation factor is

$$\begin{bmatrix} x \\ y \end{bmatrix} = \begin{bmatrix} \cos\theta & \sin\theta \\ -\sin\theta & \cos\theta \end{bmatrix} \begin{bmatrix} u \\ v \end{bmatrix}. \tag{13}$$

$\begin{bmatrix} u \\ v \end{bmatrix}$ is the new coordinate system after rotating, $u = x_n\cos\theta$ and $v = (R_0 - R_{ref}) + x_n\sin\theta$. Then, the rotated signal can be constructed as follows

$$S(K_r, K_x) = W_r(K_r) \cdot W_a(K_x)$$
$$\times \exp\begin{bmatrix} -j\left(K_x\sin\theta + \sqrt{K_r^2 - K_x^2}\cos\theta\right) \cdot v \\ -j\left(K_x\cos\theta - \sqrt{K_r^2 - K_x^2}\sin\theta\right) \cdot u \end{bmatrix}. \tag{14}$$

From (14), the first exponential term represents the range component and the second exponential term represents the azimuth component. Then, the interpolation along the cross LOS can be easily designed and yields

$$K_u = K_x \cos\theta - \sqrt{K_r^2 - K_x^2}\sin\theta \tag{15}$$

where K_u is the new azimuth wavenumber. After the interpolation, substituting (15) into (14), we have

$$SS(K_r, K_u) = W_r(K_r) \cdot W_a(K_u)$$
$$\times \exp\left[-j\sqrt{K_r^2 - K_u^2} \cdot v - jK_u \cdot u\right]. \tag{16}$$

Compared with the expression in (14), (16) is a standard spectrum form in broadside mode, which facilitates the following imaging and MoCo. In addition, Fig. 5 is the simulated spectrum of a point target in the squint mode before and after rotation, which further validates the proposed rotation operation, as described in Fig. 4.

B. Modified Stolt Interpolation

To pave the way to the following MoCo, we conduct a modified Stolt interpolation for the rotated 2-D spectrum, and the interpolation kernel is given by

$$K_v = \sqrt{K_r^2 - K_u^2} - \sqrt{K_{rc}^2 - K_u^2} \tag{17}$$

where K_v is the new range wavenumber. This kernel realizes the separation of range envelope and cross-range phase, which achieves the correction of envelope separately and protect the phase terms. This separation makes the proposed wavenumber-domain imaging algorithms combine with the MoCo methods [49]–[53] easy and the signal processed via the Stolt interpolation is

$$S(K_v, K_u) = W_r(K_v) \cdot W_a(K_u)$$
$$\times \exp\left[-j\sqrt{K_{rc}^2 - K_u^2} \cdot v - jK_u \cdot u - jK_v \cdot v\right]. \tag{18}$$

In (18), the first term is a wavenumber-domain matching factor, and the second term represents the focusing position along the cross LOS. The last term represents the range focusing position after range IFFT. It is obvious that there exists no range–azimuth coupling and the azimuth phase includes a linear term and a modulated term of K_u.

C. Wavenumber-Domain Focusing

Reviewing (18), for the conventional full-aperture imaging, 2-D focusing can be achieved via a matched filter and a subsequent 2-D IFFT. However, for subaperture data processing, as the length of the effective synthetic aperture is much smaller than the width of the scene, the conventional imaging algorithms in the time domain cannot cover all of the points in the scene. The uncovered scene will aliasing into the final imagery. In Fig. 6(a), A, B, and C are three point targets located in the same range cell but in different azimuth cells, namely u_A, u_B, and u_C. The phase-frequency distribution lines of these three targets are shown as the solid purple, solid red, and solid green lines, respectively. If the strategy of time-domain focusing is selected, the matching
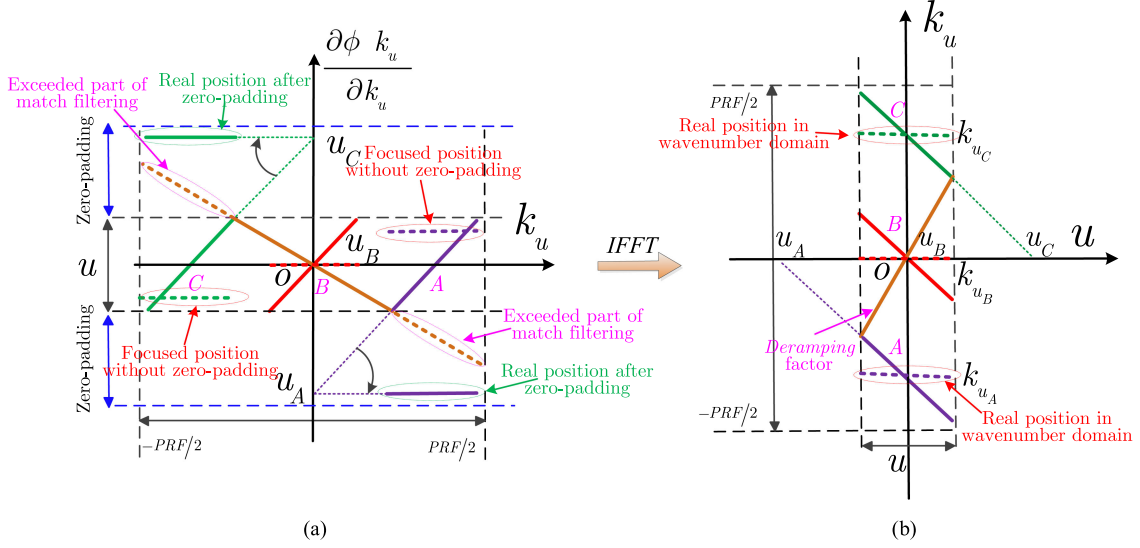
Fig. 6. Comparison of difference focusing domain. (a) Description of time-domain focusing before and after the zero-padding operation. (b) Description of wavenumber-domain focusing.

factor will exceed the length of the synthetic aperture perpendicular to the LOS, as shown by the dotted brown line in Fig. 6(a). The excessive part will be folded, and thus change the position where the targets are eventually focused without zero padding. For realizing the targets located in the real position, a large-scale zero padding is needed. However, the heavy computational cost will be brought by zero-padding operation. In order to avoid the heavy computation, the wavenumber-domain focusing is selected instead. In Fig. 6(b), the time–frequency lines of targets A, B, and C cross the u-axis are their real distance position u_A, u_B, and u_C. Now it is expected to utilize the deramping and exert azimuth FFT to focus the targets in the wavenumber domain without zero padding. The final focusing positions of targets A, B, and C are k_{u_A}, k_{u_B}, and k_{u_C}, respectively.

After the range focusing via range IFFT, it is needed to compensate for a reference factor that can restore the actual characteristics of the azimuth phase [11]. The factor is

$$H_{af}(K_u, R_{\text{ref}}) = \exp\left[-j\sqrt{K_{rc}^2 - K_u^2} \cdot R_{\text{ref}}\right] \quad (19)$$

where R_{ref} is the reference range position of targets. Multiplying (18) by (19), the expression of (18) is rearranged as

$$S(K_u, R_0) = \text{sinc}\left[B_r\left(R - (R_0 - R_{ref})\right)\right] \cdot W_a(K_u)$$
$$\times \exp\left[-j\sqrt{K_{rc}^2 - K_u^2} \cdot R_0 - jK_u \cdot u\right] \quad (20)$$

where B_r is related to the transmitted bandwidth. For the signal after range pulse compression, the phase in the azimuth wavenumber domain contains the high-order terms of K_u. Transforming (20) into the azimuth time domain, the signal can be expressed as

$$S(X, R_0) = \text{sinc}\left[B_r\left(R - (R_0 - R_{\text{ref}})\right)\right] \cdot w_a(X)$$
$$\times \exp\left[jK(R_0) \cdot (X - u)^2\right] \quad (21)$$

where $K(R_0) = \frac{-2\pi}{\lambda R_0}$ and X is the corresponding representation of K_u in azimuth time domain. From (21), to realize imaging in the azimuth wavenumber domain, the azimuth deramping operation is introduced and its factor is

$$H_{\text{deramp}}(X; R_0) = \exp\left[-jK(R_0) \cdot X^2\right]. \quad (22)$$

Then, the signal after azimuth deramping is expressed as

$$S(X, R_0) = \text{sinc}\left[B_r\left(R - (R_0 - R_{\text{ref}})\right)\right] \cdot w_a(X)$$
$$\times \exp\left[-j2K(R_0) \cdot X \cdot u\right]$$
$$\times \exp\left[jK(R_0) \cdot u^2\right]. \quad (23)$$

Obviously, there is only the linear term of the azimuth distance X, namely, the signal can be focused in the wavenumber domain by conducting azimuth FFT. The final focused signal is given by

$$S(u, R_0) = \text{sinc}\left[B_r\left(R - (R_0 - R_{\text{ref}})\right)\right]$$
$$\cdot \text{sinc}\left[B_a\left(k_u + 2K(R_0)u\right)\right]$$
$$\times \exp\left[jK(R_0) \cdot u^2\right] \quad (24)$$

where B_a is related to Doppler bandwidth. In (24), the exponential term is constant and the focused imagery in the wavenumber domain is obtained. As mentioned earlier, the focused plane of imagery is plane $BCDP$. Compared with the imagery focused on the ground plane, there is a serious geometry distortion of the focused imagery on the new imaging plane. Therefore, the final imagery in (24) should be corrected to the ground plane via geometric correction.

D. Geometric Correction via Inverse Projection

In order to remove the distortion caused by the equivalent range model, a geometric correction method via inverse projection [32] is performed. The basic idea is to display an equally spaced grid on the ground first and then calculate the range and Doppler information of the pixels in the grid corresponding to
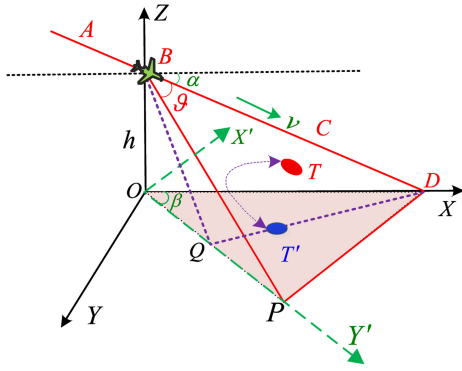
Fig. 7. Diagram for geometric correction via inverse projection.

Fig. 8. Flowchart of the proposed algorithm.

the slant range point inversely. Inverse projection uses fewer points and it is easier to be implemented in parallel compared with the conventional geometric correction method.

Suppose an arbitrary point T' located on the ground plane, and the corresponding point on the slant range plane is T, as shown in Fig. 7. The instantaneous range and Doppler information of T' can be calculated by the following range-Doppler (RD) equation

$$\begin{cases} R = \sqrt{x^2 + y^2 + h^2} \\ f_d = \frac{2v}{\lambda}\sin\theta' \end{cases} \quad (25)$$

where R, θ', and f_d represent the instantaneous range, squint angle, and instantaneous Doppler frequency of point T', respectively. $[x, y]$ is the coordinate of point T' in the XOY coordinate. The expression of θ' can be calculated by [32]

$$\theta' = \arcsin\left(\frac{h\sin\alpha + y\cos\alpha}{R}\right). \quad (26)$$

Based on the RD equation and (26), the nearest distance from point T' to the vertical LOS direction is calculated by

$$R_n = R \cdot \cos(\theta' - \theta_0) \quad (27)$$

where θ_0 is the center squint angle and is complementary to angle ϑ. Further, the norm of inverse projection is

$$\begin{cases} x = \left(\frac{f_d \cdot \lambda R}{2v\cos\alpha} - h \cdot \tan\alpha\right) \\ y = \sqrt{R^2 - h^2 - \left(\frac{f_d \cdot \lambda R}{2v\cos\alpha} - h \cdot \tan\alpha\right)^2} \end{cases}. \quad (28)$$

The value of $[x', y']$ in the range and cross-range direction is

$$\begin{bmatrix} x' \\ y' \end{bmatrix} = \begin{matrix} \sin\beta & -\cos\beta \\ \cos\beta & \sin\beta \end{matrix} \cdot \begin{bmatrix} x \\ y \end{bmatrix}. \quad (29)$$

Observing (28) and (29), the range and Doppler information of all the displayed points on the ground can be precisely calculated by the geometric model and RD information of the slant range points. Then, to calculate the nearest range R_n and Doppler f_d, a 2-D sinc interpolation algorithm is selected to ensure the accuracy, with the interpolation kernel

$$s(n, m) = \text{sinc}(n - R_n/\partial R_n) \cdot \text{sinc}(m - f_d/\partial f_d) \quad (30)$$

where ∂R and ∂f_d denote the range and cross-range intervals of the ground image, respectively. The accurate position of each

Fig. 9. Simulation model and points distribution.
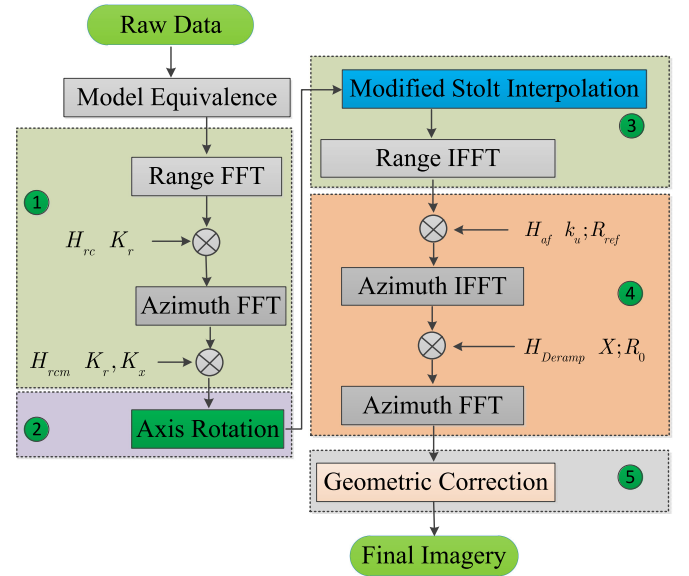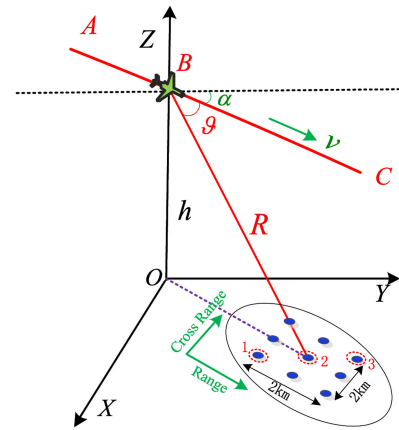
target based on the inverse projection from the ground plane to slant range plane can be calculated and the final image without distortion on the ground can be obtained.

E. Flowchart of the Whole Procedure

In the previous procedures, a modified wavenumber-domain imaging algorithm based on the equivalent range model is proposed. With the considerations of real-time processing and accuracy, a fast geometric correction by inverse projection is adopted to realize the geometric correction. In summary, the main procedures of the proposed algorithm include five parts: the range preprocessing, axis rotation, modified Stolt interpolation, wavenumber-domain focusing, and geometric correction. The flowchart of the modified wavenumber-domain imaging algorithm combined with an equivalent range model is summarized as Fig. 8.
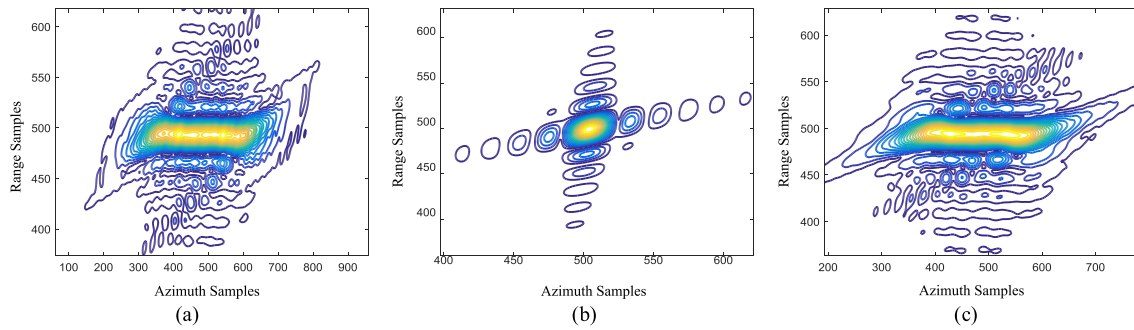
Fig. 10. Imaging results processed by the proposed algorithm with conventional range model. (a)–(c) Results of PT1–PT3, respectively.
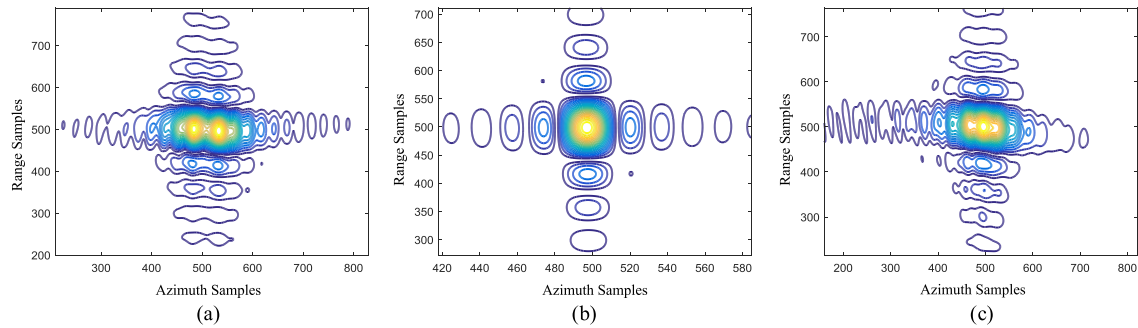

Fig. 11. Imaging results processed by the reference algorithm [33]. (a)–(c) Results of PT1–PT3, respectively.
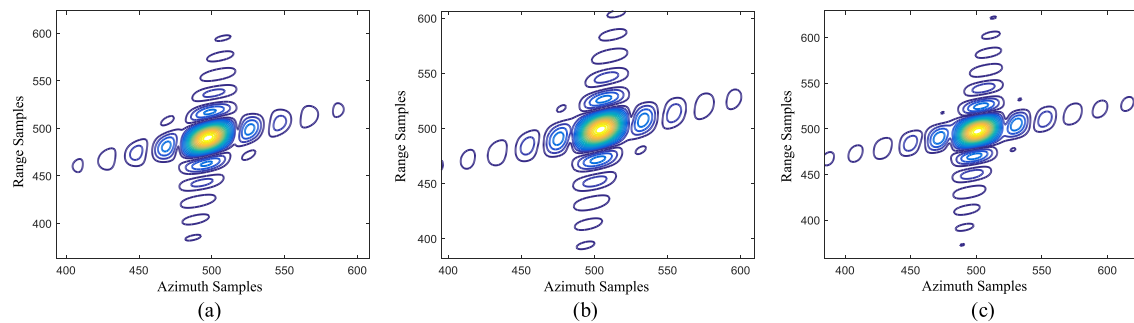

Fig. 12. Imaging results processed by the proposed algorithm. (a)–(c) Results of PT1–PT3, respectively.

IV. SIMULATION AND REAL DATA PROCESSING RESULTS

In order to evaluate the performance of the proposed algorithm, simulation data and real data results are displayed in the following parts.

A. Simulation Results

The simulation parameters are listed in Table I. Point targets of 3×3 with a size of 2×2 km are distributed on the ground. The flight path of maneuvering the SAR platform is diving with a vertical velocity, as shown in Fig. 9. Both the range and cross-range resolutions are about 0.5 m. In order to have a better comparison, we select two side points named point target one (PT1) and point target three (PT3), and middle one named point target two (PT2) as a contrast. The focusing results processed by the reference method [33] and the proposed algorithm are compared with each other in detail by the imaging results of selected PT1–PT3 (the imaging results are shown without windowing). Fig. 10 gives the imaging results of the proposed algorithm without the equivalent range model and Fig. 11 shows the reference method processed with the proposed model. Fig. 12 is the result of the proposed method.

Admittedly, both the results of PT1 and PT3 shown in Fig. 10 are defocusing due to the large approximation error of range model, while PT2 is the center point without range approximation and it has a good focusing performance. This phenomenon also happens in the reference method, which performs well for the central point PT2, while noticeable defocus appears for the edge points PT1 and PT3. This is because the reference method brings azimuth-variance, and thus leads to defocus

TABLE II
COMPARISON OF IMAGING QUALITY INDEXES WITHOUT WINDOWING

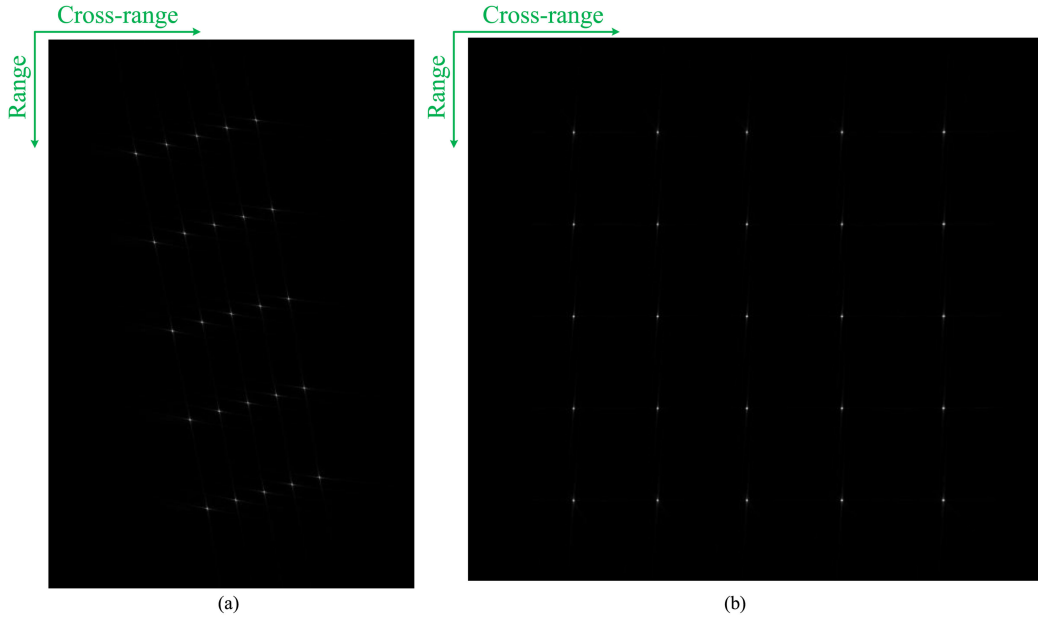| Imaging Quality Indexes	Theoretical Value	PT1	PT2	PT3	PT1	PT2	PT3
		Proposed Algorithm			Referenced Algorithm		
PSLR (dB)	-13.26	-12.73	-12.82	-13.04	-5.44	-13.25	-5.15
ISLR (dB)	-9.80	-9.65	-9.71	-9.71	-4.42	-10.64	-4.30
Resolution (m)	0.5	0.51	0.53	0.52	1.31	0.49	1.42

Fig. 13.   Imaging results before and after geometric correction. (a) Before geometric correction. (b) After geometric correction.

TABLE III
LIST OF REAL DATA PARAMETERS

System Parameters	Value	Motion Parameters	Value
Carrier frequency	16.9 GHz	Squint angle (θ)	67°
Pulse bandwidth	110 MHz	Altitude	3.5 km
Sampling frequency	150 MHz	Center slant range	15 km
Pulse duration	40 μs	Diving angle(α)	$\sim6^{o}$
System PRF	1 KHz	Velocity of platform (v)	(0,119.3,-11.5) m/s

shown Fig. 11(a) and (c). In contrast, both edge points and central points are precisely focused via the proposed algorithm. The main-lobes and side-lobes are well separated from each other and present an ideal "cross," which validates its priority.

To further evaluate the performance of the proposed algorithm, the imaging quality indexes of the simulation results are quantified as shown in Table II, which includes peak side-lobe ratio (PSLR), integrated side-lobe ratio (ISLR), and cross-range resolution. Evidently, compared with the reference algorithm, the proposed algorithm not only achieves precise focusing of the edge targets, but also satisfactory imaging quality indexes, which are specifically more similar to theoretical values of PSLR (-13.26 dB), ISLR (-9.8 dB), and spatial resolution (0.5 m).

Furthermore, a 5×5 dot matrix is arranged in the scene and Fig. 13(a) gives the imaging result in the slant range plane. It is clear that there is a large distort compared with the placed dot matrix. Fig. 13(b) shows the imagery after geometric correction, which meets the arranged lattice.

B. Real Data Processing Results

The airborne raw data of maneuvering high-squint-mode SAR are processed to validate the effectiveness of the proposed algorithm. The bandwidth of the transmitted signal is 110 MHz and the platform velocity is about 120 m/s with a diving angle $\sim5°$. The slant range and flight height are 15 km and 3.5 km, respectively. The whole scene is 3 km in the range and 1 km in the cross range, and the resolutions in the range and the cross range are both about 1.5 m. The detailed parameters are listed in Table III. The imaging results are displayed in Fig. 14. Specifically, Fig. 14(b) obtained by the proposed algorithm is of
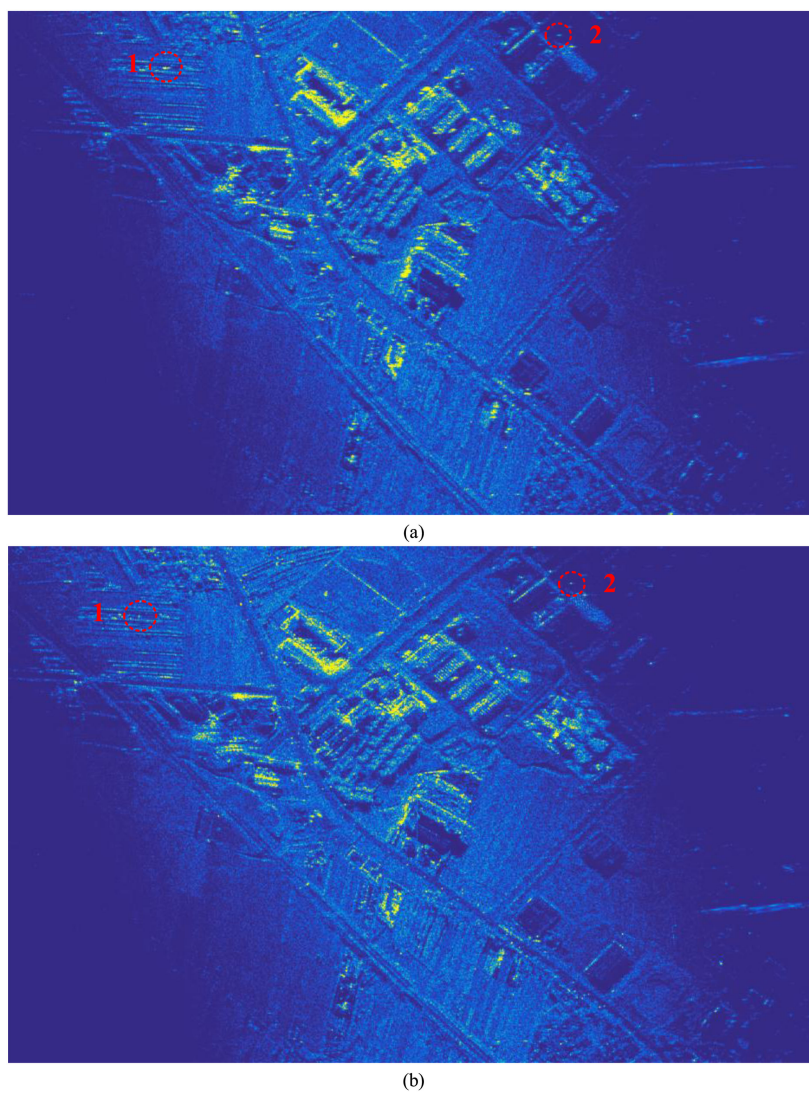
Fig. 14. Imaging results of real data. (a) Image acquired by the reference method [33]. (b) Image acquired by the proposed method.
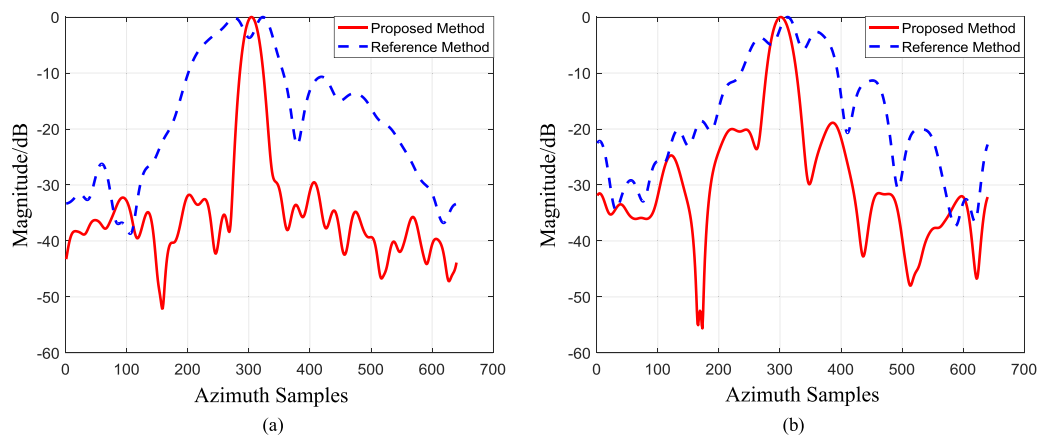

Fig. 15. Profiles of the selected points. (a) Profile of point 1. (b) Profile of point 2.
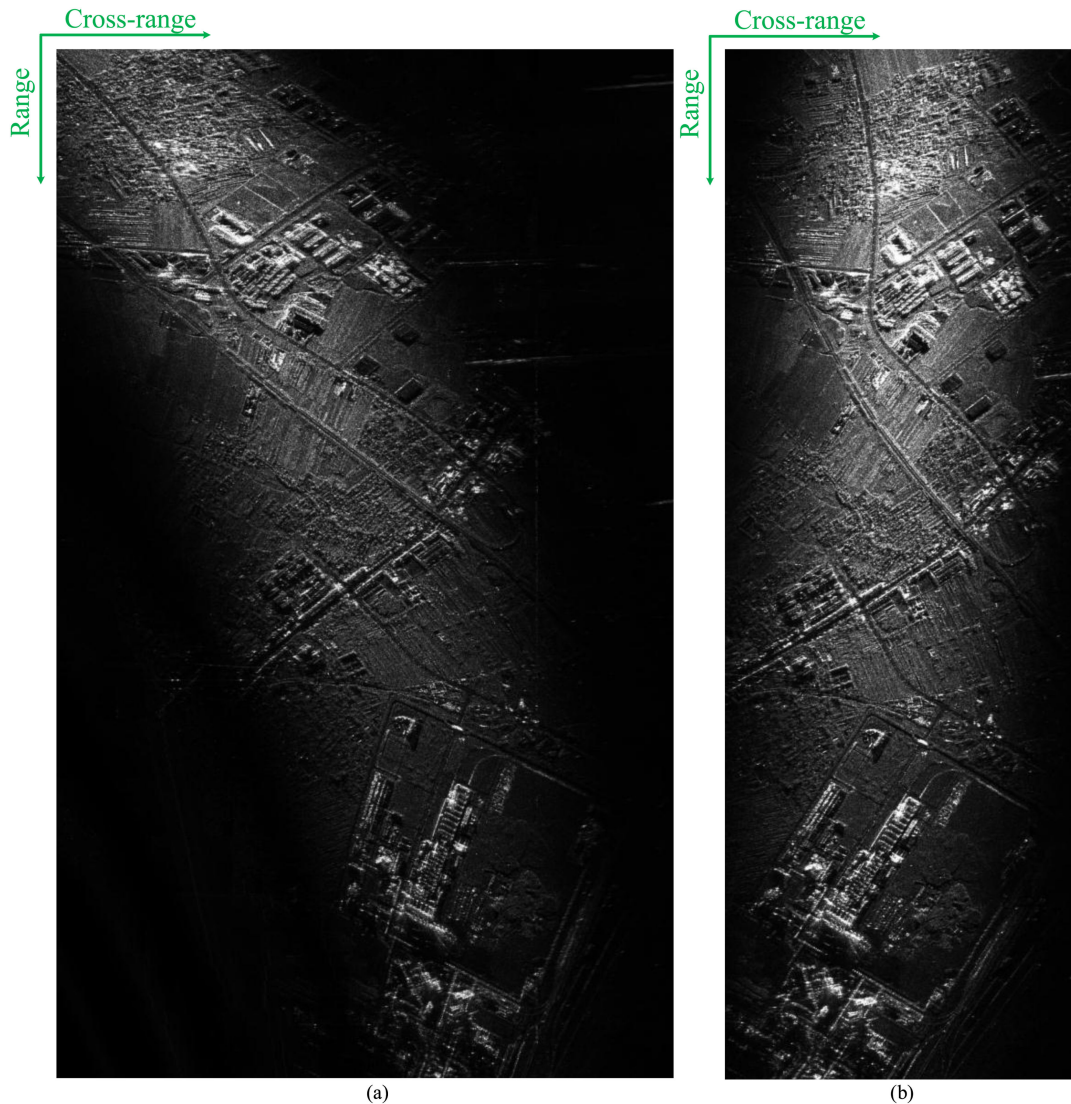
Fig. 16.   Imaging results of geometric correction. (a) Image result before geometric correction. (b) Image result after geometric correction.

higher quality than of Fig. 14(a) corresponding to the reference algorithm [33].

Further, two isolated strong-scattering points at the edge of the imaging scene are selected for contrasts, which are highlighted with the red circle in Fig. 14. We extract the profile of these two points along the cross range direction, as shown in Fig. 15. The red line in Fig. 15 is the cross range focusing result obtained by the proposed algorithm and the blue line is the result acquired by reference [33]. Evidently, energy is focused precisely on the selected points processed by the proposed algorithm, for the narrower main-lobe width of the red line. In contrast, for the reference algorithm as mentioned above, the azimuth chirp rate is mismatched and the defocus of energy emerges shown as the blue line in Fig. 15.

Finally, Fig. 16 shows the results before and after the geometric correction. In Fig. 16(a), the imaging result on the slant range plane is distorted, which looks like a curved "parallelogram" shown as the simulation result in Fig. 13(a). After the geometric correction, the imaging result on the ground plane is obtained

in Fig. 16(b). The whole results demonstrate the feasibility of geometric correction.

V. CONCLUSION

In this article, a modified imaging algorithm combined with an equivalent range model is proposed for maneuvering high-squint-mode SAR. First, the advantages of the equivalent geo-metric model of maneuvering flight paths are analyzed compared with the conventional slant range model. Especially on the new imaging plane, the azimuth-shift invariance is still satisfactory along the cross range direction. Then, a wavenumber-domain imaging algorithm is proposed. Its main innovation is to obtain the axis rotation and modified Stolt interpolation, which pre-serves the resolution of images and makes it easy to combine withMoCo. In addition, with the consideration of real-time processing and resolution requirements, the subaperture data are focused on a new focusing domain, i.e., the wavenumber domain, which avoids the complex zero padding of conventional

focusing methods. The processed results of simulated data and real data validate the priority of the proposed algorithm.

Acknowledgment

References

[1] I. G. Cumming and F. H. Wong, *Digital Processing of Synthetic Aperture Radar Data: Algorithms and Implementation*. Boston, MA, USA: Artech House, 2005.

[2] L. Zhang, J. Sheng, M. Xing, Z. Qiao, T. Xiong, and Z. Bao, "Wavenumber-domain autofocusing for highly squinted UAV SAR imagery," *IEEE Sens. J.*, vol. 12, no. 5, pp. 1574–1588, May 2012.

[3] L. Zhang, Z. Qiao, M. Xing, L. Yang, and Z. Bao "A robust motion compensation approach for UAV SAR imagery," *IEEE Trans. Geosci. Remote Sens.*, vol. 50, no. 8, pp. 3202–3218, Aug. 2012.

[4] S. Tang, L. Zhang, P. Guo, and Y. Zhao, "An omega-K algorithm for highly squinted missile-borne SAR with constant acceleration," *IEEE Geosci. Remote Sens. Lett.*, vol. 11, no. 9, pp. 1569–1573, Sep. 2014.

[5] S. Chen, H. Zhao, S. Zhang, and Y. Chen, "An extended nonlinear chirp scaling algorithm for missile borne SAR imaging," *Signal Process.*, vol. 99, pp. 58–68, Jun. 2014.

[6] Y. Liang, Z.Y. Li, L. Zeng, M. Xing, and Z. Bao, "A high order phase correction approach for focusing HS-SAR small-aperture data of high-speed moving platforms," *IEEE J. Sel. Topics Appl. Earth Observ. Remote Sens.*, vol. 8, no. 9, pp. 4551–4561, Sep. 2015.

[7] S.-Xi Zhang, M.-D. Xing, X.-G. Xia, L. Zhang, R. Guo, and Z. Bao "Focus improvement of high-squint SAR based on Azimuth dependence of quadratic range cell migration correction," *IEEE Geosci. Remote Sens. Lett.*, vol. 10, no. 1, pp. 150–154, Jan. 2013.

[8] F. H. Wong and T. S. Yeo, "New applications of nonlinear chirp scaling in SAR data processing," *IEEE Trans. Geosci. Remote Sens.*, vol. 39, no. 5, pp. 946–953, May 2001.

[9] G. Sun, M. Xing, Y. Liu, L. Sun, Z. Bao, and Y. Wu, "Extended NCS based on method of series reversion for imaging of highly squinted SAR," *IEEE Geosci. Remote Sens. Lett.*, vol. 8, no. 3, pp. 446–450, May 2011.

[10] Z. Li, Y. Liang, M. Xing, Y. Huai, L. Zeng, and Z. Bao, "Focusing of highly squinted SAR data with frequency nonlinear chirp scaling," *IEEE Geosci. Remote Sens. Lett.*, vol. 13, no. 1, pp. 23–27, Jan. 2016.

[11] Y. Liang, Y. Huai, J. Ding, H. Wang, and M. Xing, "A modified ω–k algorithm for HS-SAR small-aperture data imaging," *IEEE Trans. Geosci. Remote Sens.*, vol. 54, no. 6, pp. 3710–3721, Jun. 2016.

[12] G. Sun, X. Jiang, M. Xing, Z. Qiao, Y. Wu, and Z. Bao, "Focus improvement of highly squinted data based on Azimuth nonlinear scaling," *IEEE Trans. Geosci. Remote Sens.*, vol. 49, no. 6, pp. 2308–2322, Jun. 2011.

[13] D. An, X. Huang, T. Jin, and Z. Zhou, "Extended nonlinear chirp scaling algorithm for high-resolution highly squint SAR data focusing," *IEEE Trans. Geosci. Remote Sens.*, vol. 50, no. 9, pp. 3595–3609, Sep. 2012.

[14] L. Gaogao, P. Li, S. Tang, and L. Zhang, "Focusing highly squinted data with motion errors based on modified non-linear chirp scaling," *IET Radar Sonar Navig.*, vol. 7, no. 5, pp. 568–578, Jun. 2013.

[15] O. Frey, C. Magnard, M. Ruegg, and E. Meier, "Focusing of airborne synthetic aperture radar data from highly nonlinear flight tracks," *IEEE Trans. Geosci. Remote Sens.*, vol. 47, no. 6, pp. 1844–1858, Jun. 2009.

[16] B. Deng, X. Li, H. Wang, Y. Qin, and J. Wang, "Fast raw signal simulation of extended scenes for missile-borne SAR with constant acceleration," *IEEE Geosci. Remote Sens. Lett.*, vol. 8, no. 1, pp. 44–49, Jan. 2011.

[17] S. Tang, L. Zhang, P. Guo, G. Liu, and G.-C. Sun, "Acceleration model analyses and imaging algorithm for highly squinted airborne spotlight-mode SAR with maneuvers," *IEEE J. Sel. Topics Appl. Earth Observ. Remote Sens.*, vol. 8, no. 3, pp. 1120–1131, Mar. 2015.

[18] Z. Li *et al.*, "An improved range model and omega-k-based imaging algorithm for high-squint SAR with curved trajectory and constant acceleration," *IEEE Geosci. Remote Sens. Lett.*, vol. 13, no. 5, pp. 656–660, May 2016.

[19] T. Zeng, Y. Li, Z. Ding, T. Long, D Yao, and Y. Sun, "Subaperture approach based on Azimuth-dependent range cell migration correction and azimuth focusing parameter equalization for maneuvering high-squint-mode SAR," *IEEE Trans. Geosci. Remote Sens.*, vol. 52, no. 12, pp. 6718–6734, Dec. 2015.

[20] J. Yang, G. Sun, M. Xing, X.-G. Xia, Y. Liang, and Z. Bao, "Squinted TOPS SAR imaging based on modified range migration algorithm and spectral analysis," *IEEE Geosci. Remote Sens. Lett.*, vol. 11, no. 10, pp. 1707–1711, Oct. 2014.

[21] G. Xu, M. Xing, L. Zhang, and Z. Bao, "Robust autofocusing approach for highly squinted SAR imagery using the extended wavenumber algorithm," *IEEE Trans. Geosci. Remote Sens.*, vol 51, no. 10, pp. 5031–5046, Oct. 2013.

[22] K. Eldhuset, "A new fourth-order processing algorithm for spaceborne SAR," *IEEE Trans. Aerosp. Electron. Syst.*, vol. 34, no. 3, pp. 824–835, Jul. 1998.

[23] L. Huang, X. Qiu, D. Hu, and C. Ding, "Focusing of medium-earth-orbit SAR with advanced nonlinear chirp scaling algorithm," *IEEE Trans. Geosci. Remote Sens.*, vol. 49, no. 1, pp. 500–508, Jan. 2011.

[24] Y. Luo, B. Zhao, X. Han, R. Wang, H. Song, and Y. Deng, "A novel high-order range model and imaging approach for high-resolution LEO SAR," *IEEE Trans. Geosci. Remote Sens.*, vol. 52, no. 6, pp. 3473–3485, Jun. 2014.

[25] M. Bao, M. D. Xing, Y. Wang, and Y. C. Li, "Two-dimensional spectrum for MEO SAR processing using a modified advanced hyperbolic range equation," *Electron. Lett.*, vol. 47, no. 18, pp. 1043–1045, Sep. 2011.

[26] Z. Li, Y Liang, M. Xing, Y. Gao, and J. Chen, "An equivalent range model for synthetic aperture radar with curved track," *Electron. Lett.*, vol. 52, no. 14, pp. 1252–1253, Jul. 2016.

[27] Y. Wu, G.-C. Sun, C. Yang, J. Yang, M. Xing, and Z. Bao, "Processing of very high resolution spaceborne sliding spotlight SAR data using velocity scaling," *IEEE Trans. Geosci. Remote Sens.*, vol. 54, no. 3, pp. 1505–1518, Mar. 2016.

[28] P. Wang, W. Liu, J. Chen, M. Niu, and W. Yang, "A high-order imaging algorithm for high-resolution spaceborne SAR based on a modified equivalent squint range model," *IEEE Trans. Geosci. Remote Sens.*, vol. 53, no. 3, pp. 1225–1235, Mar. 2015.

[29] G.-C. Sun, M. Xing, Y. Wang, J. Yang, and Z. Bao, "A 2-D space-variant chirp scaling algorithm based on the RCM equalization and sub-band synthesis to process geosynchronous SAR data," *IEEE Trans. Geosci. Remote Sens.*, vol. 52, no. 8, pp. 4868–4880, Aug. 2014.

[30] P. Zhou, M. Xing, T. Xiong, Y. Wang, and L. Zhang, "A variable-decoupling and MSR-based imaging algorithm for a SAR of curvilinear orbit," *IEEE Geosci. Remote Sens. Lett.*, vol. 8, no. 6, pp. 1145–1149, Nov. 2011.

[31] S. Tang "Processing of monostatic SAR data with general configurations," *IEEE Trans. Geosci. Remote Sens.*, vol. 53, no. 12, pp. 6529–6546, Dec. 2015.

[32] Z. Li, "A frequency-domain imaging algorithm for highly squinted SAR mounted on maneuvering platforms with nonlinear trajectory," *IEEE Trans. Geosci. Remote Sens.*, vol. 54, no. 7, pp. 4023–4038, Jul. 2016.

[33] Y Liang, Y. Dang, G. Li, J. Wu, and M. Xing, "A two-step processing method for diving mode squint SAR imaging with sub-aperture data," *IEEE Trans. Geosci. Remote Sens.*, vol. 58, no. 2, pp. 811–825, Feb. 2020.

[34] Z. Ding, W. Yin, T. Zeng, and T. Long, "Radar parameter design for geosynchronous SAR in squint mode and elliptical orbit," *IEEE J. Sel. Topics Appl. Earth Observ. Remote Sens.*, vol. 9, no. 6, pp. 2720–2732, Jun. 2016.

[35] B. Bie "A frequency domain backprojection algorithm based on local cartesian coordinate and subregion range migration correction for high-squint SAR mounted on maneuvering platforms," *IEEE Trans. Geosci. Remote Sens.*, vol. 56, no. 12, pp. 7086–7101, Dec. 2018.

[36] Y. Dang, Y. Liang, B. Bie, J. Ding, and Y. Zhang, "A range perturbation approach for correcting spatially variant range envelope in diving highly squinted SAR with nonlinear trajectory," *IEEE Geosci. Remote Sens. Lett.*, vol. 15, no. 6, pp. 858–862, Jun. 2018.

[37] B. Bie, G.-C. Sun, X.-G. Xia, M. Xing, Z. Bao, and L. Gu, "High-speed maneuvering platforms squint beam-steering SAR imaging without subaperture," *IEEE Trans. Geosci. Remote Sens.*, vol. 57, no. 9, pp. 6974–6985, Sep. 2019.

[38] Z. Zhou, Z. Ding, T. Zeng, G. Li, and L. Li, "Novel acceleration compensation method for highly squint mode SAR with curve trajectory," *J. Eng.*, vol. 2019, no. 20, pp. 6527–6532, 2019.

[39] G. Li, Y. Ma, L. Shi, and J. Hou, "KT and Azimuth sub-region deramp-based high-squint SAR imaging algorithm mounted on maneuvering platforms," *IET Radar, Sonar Navig.*, vol. 14, no. 3, pp. 388–398, Mar. 2020.

[40] L. Yachao, D. Huan, Q. Yinghui, L Chunbiao, and X. Mengdao, "Sequence design for high squint spotlight SAR imaging on manoeuvring descending trajectory," *IET Radar, Sonar Navig.*, vol. 11, no. 2, pp. 219–225, Feb. 2017.

[41] B. Huang, S. Zhang, W.-Q. Wang, T. Liao, D. Du, and X. Zhao, "High-precision imaging algorithm for highly squinted SAR with 3-D acceleration," *IEEE Access*, vol. 7, pp. 130399–130409, 2019.

[42] L. M. H. Ulander, H. Hellsten, and G Stenström, "Synthetic aperture radar processing using fast factorized back-projection," *IEEE Trans. Aerosp. Electron. Syst.*, vol. 39, no. 3, pp. 760–776, Jul. 2003.

[43] L. Zhang, H.-L. Li, Z.-J. Qiao, and Z.-W. Xu, "A fast BP algorithm with wavenumber spectrum fusion for high-resolution spotlight SAR imaging," *IEEE Geosci. Remote Sens. Lett.*, vol. 11, no. 9, pp. 1460–1464, Jan. 2014.

[44] L. Ran, Z. Liu, T. Li, R. Xie, and L. Zhang, "An adaptive fast factorized back-projection algorithm with integrated target detection technique for high-resolution and high-squint spotlight SAR imagery," *IEEE J. Sel. Topics Appl. Earth Obs. Remote Sens.*, vol. 11, no. 1, pp. 171–183. Jan. 2018.

[45] L. Ran, Z. Liu, L. Zhang, R. Xie, and T. Li, "Multiple local autofocus back-projection algorithm for space-variant phase-error correction in synthetic aperture radar," *IEEE Geosci. Remote Sens. Lett.*, vol. 13, no. 9, pp. 1241–1245. Sep. 2016.

[46] S. Jun, M. Long, and X. L Zhang, "Streaming BP for non-linear motion compensation SAR imaging based on GPU," *IEEE J. Sel. Topics Appl. Earth Obs. Remote Sens.*, vol. 6, no. 4, pp. 2035–2050, Apr. 2013.

[47] L. Yang, L. Zhao, S. Zhou, G. Bi, and H. Yang, "Spectrum-oriented FFBP algorithm in quasi-polar grid for SAR imaging on maneuvering platform," *IEEE Geosci. Remote Sens. Lett.*, vol. 14, no. 5, pp. 724–728, May 2017.

[48] A. Reigber, E. Alivizatos, A. Potsis, and A. Moreira, "Extended wavenumber-domain synthetic aperture radar focusing with integrated motion compensation," *IEE Proc., Radar Sonar Navig.*, vol. 153, no. 3, pp. 301–310, Jun. 2006.

[49] L. Zeng, Y. Liang, M. Xing, Y. Huai, and Z. Li, "A novel motion compensation approach for airborne spotlight SAR of high-resolution and high-squint mode," *IEEE Geosci. Remote Sens. Lett.*, vol. 13, no. 3, pp. 429–433, Mar. 2016.

[50] M. Xing, X. Jiang, R. Wu, F. Zhou, and Z. Bao, "Motion compensation for UAV SAR based on raw radar data," *IEEE Trans. Geosci. Remote Sens.*, vol. 47, no. 8, pp. 2870–2883, Aug. 2009.

[51] J. Chen, M. Xing, G.-C. Sun, and Z. Li, "A 2-D space-variant motion estimation and compensation method for ultrahigh-resolution airborne stepped-frequency SAR with long integration time," *IEEE Trans. Geosci. Remote Sens.*, vol. 55, no. 11, pp. 6390–6401, Nov. 2017.

[52] J. Chen, B. Liang, D.-G. Yang, D.-J. Zhao, G.-C. Sun, and M. Xing, "Two-step accuracy improvement of motion compensation for airborne SAR with ultrahigh resolution and wide swath," *IEEE Trans. Geosci. Remote Sens.*, vol. 57, no. 9, pp. 7148–7160, Sep. 2019.

[53] L. Ran, R. Xie, Z. Liu, L. Zhang, T. Li, and J. Wang, "Simultaneous range and cross-range variant phase error estimation and compensation for highly-squinted SAR imaging," *IEEE Trans. Geosci. Remote Sens.*, vol. 56, no. 8, pp. 4448–4463, Aug. 2018.

Wentao Du was born in Chaohu, Anhui Province, China, in 1989. He received the B.S. and Ph.D. degrees in electronic engineering from Xidian University, Xi'an, China, in 2010 and 2015, respectively.

He is currently an Engineer with the Nanjing Research Institute of Electronics Technology, Nanjing, China. His research interests include synthetic aperture radar (SAR) imaging and ground moving target indication (GMTI).

Bing Gao was born in YuXi, Yunnan Province, China, in 1981. He received the B.S. and M.D. degrees from Tsinghua University, Beijing, China, in 2005 and 2007, respectively.

He is currently working on radar system design with the Nanjing Research Institute of Electronics Technology, Nanjing, China. His research interests include radar system architecture design and antijamming design.

Deming Guo was born in Yiyang, Hunan Province, China, in 1984. He received the B.S. degree from Jilin University, Changchun, China, in 2006 and the Ph.D. degree in electronic engineering from Beihang University, Beijing, China, in 2011.

He is currently working in radar system and radar signal processing at the Nanjing Research Institute of Electronics Technology, Nanjing, China. His research interests include synthetic aperture radar (SAR) imaging and airborne radar system.

Zhenyu Li was born in Lu'an, Anhui Province, China, in 1991. He received the B.S. and Ph.D. degrees in electronic engineering from Xidian University, Xi'an, China, in 2012 and 2017, respectively.

He is currently an Engineer with the Nanjing Research Institute of Electronics Technology, Nanjing, China. His research interests include synthetic aperture radar (SAR) imaging and radar forward-looking imaging.

Dr. Li is a Reviewer of the IEEE TRANSACTIONS ON GEOSCIENCE AND REMOTE SENSING, IEEE SENSORS JOURNAL, IEEE GEOSCIENCE AND REMOTE SENSING LETTERS, IEEE SENSORS LETTERS, JOURNAL OF APPLIED REMOTE SENSING, and so on.

Tao Jiang was born in Dangtu, Anhui Province, China, in 1982. He received the B.S. degree from Tiangong University, Tianjin, China, in 2005, and the Ph.D. degree in electronic engineering from the University of Science and Technology of China, Hefei, China, in 2010.

He is currently a Deputy Minister of the Nanjing Research Institute of Electronics Technology. His research interests include synthetic aperture radar (SAR) system and new radar technology.

Jianlai Chen was born in Hengyang, Hunan Province, China, in 1990. He received the B.S. degree in electronic engineering and the Ph.D. degree in signal and information processing from Xidian University, Xi'an, China, in 2013 and 2018, respectively.

He is currently an Associate Professor with Central South University (CSU), Changsha, China. He has authored or coauthored one book and more than 20 papers. His research interests include synthetic aperture radar (SAR) imaging, geosynchronous SAR, and ultrahigh-resolution SAR.

Tao Wu was born in Yancheng, Jiangsu Province, China, in 1975. He received the B.S. degree in electronic engineering from the Nanjing University of Science and Technology, Nanjing, China, in 1997. He is currently a Deputy Minister of the Nanjing Research Institute of Electronics Technology, Nanjing, China. His research focuses on airborne radar system.

Huaigen Zhang was born in Nantong, Jiangsu Province, China, in 1980. He received the Ph.D. degree in electronic engineering from Xidian University, Xi'an, China, in 2008.

He is the Chief Expert in the field of airborne radar with the Nanjing Research Institute of Electronics Technology, Nanjing, China. His research interests include airborne radar system and radar signal processing.

Mengdao Xing (Fellow, IEEE) received the B.S. and Ph.D. degrees from Xidian University, Xi'an, China, in 1997 and 2002, respectively.

He is currently a Professor with the National Laboratory of Radar Signal Processing, Xidian University. He is also an Associate Dean of the Academy of Advanced Interdisciplinary Research. He has authored or authored more than 200 refereed scientific journal papers. He also has authored or co-authored two books about SAR signal processing. He has authored more than 40 authorized China patents. His current research interests are synthetic aperture radar (SAR), inversed synthetic aperture radar (ISAR), sparse signal processing, and microwave remote sensing.

Dr. Xing is currently the Associate Editor for radar remote sensing of the IEEE TRANSACTIONS ON GEOSCIENCE AND REMOTE SENSING. The total citation times of his research are greater than 8000. He was rated as Most Cited Chinese Researchers by Elsevier. His research has been supported by various funding programs, such as National Science Fund for Distinguished Young Scholars.